Research Article | Vol. 61, No. 9 / 20 March 2022 / Applied Optics 2417

applied optics

Wavelength tuning robustness optimization for a high-temperature single-mode VCSEL used in chip-scale atomic sensing systems

Yinli Zhou,[1] Xing Zhang,[1,2,*] Jianwei Zhang,[1] Jinjiang Cui,[3,4] Yongqiang Ning,[1] Yugang Zeng,[1] and Lijun Wang[1]

[1]State Key Laboratory of Luminescence and Applications, Changchun Institute of Optics, Fine Mechanics and Physics, Chinese Academy of Sciences, Changchun 130031, China
[2]Ace Photonics, Co., Ltd., Changchun 130031, China
[3]Suzhou Institute of Biomedical Engineering and Technology, Chinese Academy of Sciences, Suzhou 215000, China
[4]Jinan Guoke Medical Science & Technology Development Co., Ltd., Jinan 250000, China
*Corresponding author: zhangx@ciomp.ac.cn

Received 8 December 2021; revised 13 February 2022; accepted 21 February 2022; posted 23 February 2022 (Doc. ID 450782); published 17 March 2022

In this paper, the wavelength current tuning characteristics of high-temperature-operation single-mode vertical-cavity surface-emitting lasers (VCSELs) for chip-scale atomic sensing systems are studied. Excellent wavelength current tuning robustness is helpful to improve the stability of atomic sensing systems. By optimizing the size of the oxide aperture combined with surface relief mode control technology, the single-mode VCSEL with an 8 μm oxide aperture can achieve 2.02 mW output power at 355 K, and the wavelength current tuning coefficient is ∼0.25 nm/mA. This excellent wavelength current tuning robustness results from the low active current density and device heat generation due to the optimized oxide aperture size.

https://doi.org/10.1364/AO.450782

1. INTRODUCTION

Vertical-cavity surface-emitting lasers (VCSELs) are unique semiconductor lasers with the advantages of surface emission, low threshold current, and small power consumption [1,2]. Single-transverse-mode VCSELs (SM-VCSELs) are preferred optical sources for small low-power atomic sensors, including chip-scale atomic clocks, magnetometers, and gyroscopes [3]. VCSELs for these atomic sensors must meet critical requirements [4–7]. An important property is the robustness of wavelength tuning. The atomic sensing system scans the working current of VCSELs to find the working point precisely matching the alkali metal atomic absorption peak. The better the wavelength tuning robustness of VCSELs, the lower the requirement of current control precision of atomic sensor systems.

To achieve single-mode operation, the oxide aperture diameter of a traditional oxide confined VCSEL is generally <4 μm. The wavelength current tuning rate of this small oxide aperture VCSEL is ∼1.1 nm/mA [8,9]. A small oxide aperture suffers from high current density and heat generation in the active region. The device temperature increases rapidly with the increase in injection current, resulting in degeneration of wavelength current tuning characteristics.

A large oxide aperture helps to reduce the current density and temperature of the device to improve the wavelength current tuning characteristics while degrading single-mode stability due to the existence of higher-order modes. Therefore, various alternative approaches have been investigated to achieve high single-mode output power with aperture diameters larger than 4 μm; such approaches include photonic crystal or hole-structure integrated VCSELs [10,11], antiresonant reflecting optical waveguide VCSELs [12], Zn-diffusion VCSELs [13], and VCSELs with surface relief [14]. A single-mode output power of 6.5 mW at room temperature was achieved from an 850 nm VCSEL with a shallow surface relief, and a wavelength current tuning rate of ∼0.5 nm/mA with 6 μm oxide aperture was obtained [15]. By using a photonic crystal structure, a VCSEL with a 20 μm oxide aperture can achieve single-mode operation with a wavelength current tuning rate of ∼0.2 nm/mA [16]. Antiresonant reflecting optical waveguide VCSELs realized a wavelength current tuning rate of ∼0.7 nm/mA with 6 μm oxide apertures [17]. The above reports indicate that a large oxide aperture can improve the wavelength current tuning robustness of VCSELs. However, the sizes of the oxide apertures used are different, lacking unified standards and relevant studies.

To improve the wavelength current tuning characteristics of SM-VCSELs at high temperatures, this study analyzes the influence of oxide aperture diameter on the temperature characteristics of VCSELs. First, the basic structure of VCSELs is described, and an electrothermal numerical simulator including a heat equation solver is established. The simulation results are discussed. Last, experimental samples with different oxide aperture diameters are prepared, and device performances are compared.

2. DEVICE STRUCTURE AND SIMULATION ANALYSIS

A. Device Structure

The epitaxial structures of the two groups of SM-VCSELs are identical. A schematic of the epitaxial and device structure is shown in Fig. 1. N-DBR and P-distributed Bragg reflector (DBR) consist of 34.5 pairs and 22 pairs of $Al_{0.12}Ga_{0.88}As/Al_{0.9}Ga_{0.1}As$ layers, respectively. The active region is composed of three compressively strained $In_{0.06}Ga_{0.94}As$ quantum wells with a gain spectrum peak of 894 nm at 300 K. The oxide layer is realized by a 30 nm thick $Al_{0.98}Ga_{0.02}As$ layer inserted between the active region and P-DBR. After wet oxidation, a part of $Al_{0.98}Ga_{0.02}As$ is transformed into amorphous $(Al_xGa_{1-x})_2O_3$ to form the oxide aperture. As shown in Fig. 1(a), the oxide aperture diameter of the VCSEL is 8 μm. To suppress high-order-mode lasing, a common surface relief technique with a diameter of 5 μm is used. The surface relief is obtained by etching an annular groove with depth of ~63 nm on the upper surface of the VCSEL. Figure 1(b) shows the device structure of the control group with a 3 μm small oxide aperture diameter and no surface relief.

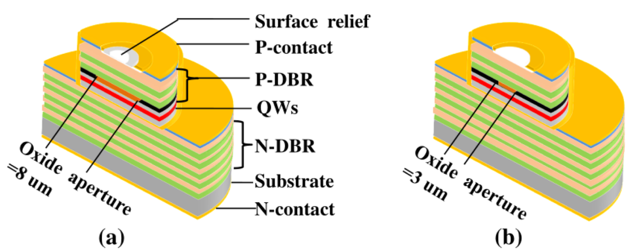

Fig. 1. Schematic of VCSELs with (a) large oxide aperture and surface relief and (b) small oxide aperture.

B. Electrothermal Model

Heating is an important factor that affects VCSEL operation (e.g., drop in optical gain and increase in carrier leakage) and leads to a decrease in photoelectric conversion efficiency. At steady state, the thermal diffusion equation to be solved is in the following form:

$$\rho C \nabla T + \nabla \cdot (-\kappa \nabla T) = Q_{\mathrm{tot}}, \tag{1}$$

where ρ is the material density, C is the specific heat capacity, T is the temperature, and κ is thermal conductivity. Four kinds of thermal behavior contribute to the total heat source Q_{tot} in VCSELs: Joule effect, optical absorption, nonradiative recombination, and carrier capture/escape [18]:

$$\begin{cases} Q_{\mathrm{tot}} = Q_{\mathrm{joule}} + Q_{\mathrm{optical}} + Q_{\mathrm{rec.}} + Q_{\mathrm{capt./esc.}} \\ Q_{\mathrm{joule}} = \sigma^{-1} \| J \|^2 \\ Q_{\mathrm{optical}} = \alpha W_{\mathrm{opt}} \\ Q_{\mathrm{rec.}} = E_g R_{\mathrm{nr}} \\ Q_{\mathrm{capt./esc.}} = \Delta_{C/V} C^{\mathrm{cap}} \end{cases}, \tag{2}$$

where σ is electrical conductivity, J is the current density, α is the internal loss due to intraband and free-carrier absorption, R_{nr} includes Shockley–Read–Hall and Auger recombinations, E_g is the bandgap, $\Delta_{C/V}$ is conduction/valence band offsets, and C_{cap} is the carrier capture/escape rate. A 2D axisymmetric model based on finite the element method is established using COMSOL Multiphysics. The bottom and top DBRs are substituted with an effective medium to simplify the calculation. This approach is widely used and has been proven to have no effect on simulation results [19,20]. The substrate thickness is set to 30 μm. The VCSEL chip is packaged in TO form after preparation. The lower surface of the chip is in contact with an AlN heat sink, and the temperature of the AlN heat sink is controlled by thermoelectric cooler (TEC). The rest of the surface of the device is exposed to air. The boundary conditions in the model are all set as convection boundary conditions, the partial heat transfer coefficient in contact with air is set as 0.012 $W/(m^2{\cdot}K)$, and the ambient temperature is set as 300 K. The heat transfer coefficient of the lower surface of VCSEL in contact with the AlN heat sink is set as 150 $W/(m^2{\cdot}K)$, and the heat sink temperature can be set according to specific requirements. The parameters of the DBR regions are fitted to account for structure simplification. The internal loss α is set to 8 cm^{-1} according to our test experience of the device. Table 1 [21] shows the main material parameters used in thermal simulation.

Table 1. Material Parameters in Thermal Simulation at 300 K

Layers	Conductivity, σ, $(\Omega{\cdot}m)^{-1}$	Thermal Conductivity, κ, (W/m/K)	Capacity, C, (J/kg/K)	Material Density, ρ, (kg/m^3)	Reference
P-electrode	1×10^7	300	132.2	1.93×10^4	[21]
P-DBR	445.4	54.29	375.5	4.53×10^3	fit
Active layer	120	43.75	332	5.39×10^3	[21]
N-DBR	739.2	54.29	375.5	4.53×10^3	fit
Substrate	4.5×10^4	45	327	5.32×10^3	[21]
N-electrode	1×10^7	300	132.2	1.93×10^4	[21]

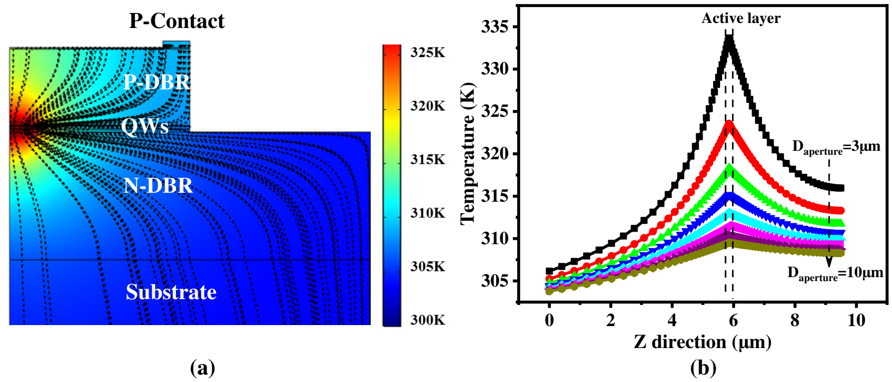

Fig. 2. (a) Color graphic of the temperature distribution in a cross-sectional plane of a 3 μm oxide aperture diameter VCSEL at 3 mA and 300 K. (b) Temperature distribution along the epitaxial direction of VCSEL at 300 K with different oxide aperture diameters.

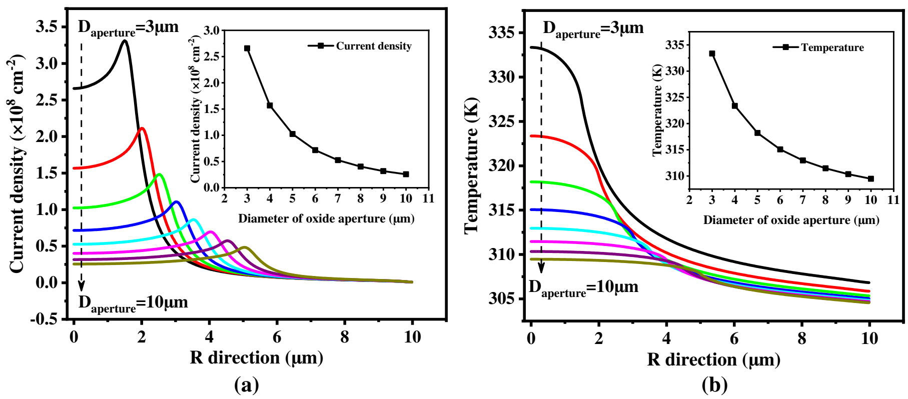

Fig. 3. Surface current density and temperature distribution of VCSELs along the r direction with different oxide aperture diameters at 3 mA. The heat sink temperature is 300 K.

C. Numerical Simulation Results

A colorgraphic of the temperature distribution in a cross-sectional plane ($r-z$ plane), i.e., 3 μm oxide aperture diameter VCSEL, is given in Fig. 2(a). The continuous wave (CW) injection current is 3 mA, and the temperature of the lower surface of the VCSEL (or heat sink) is set to 300 K. The black arrows represent the direction of the current vector. The current crowding effect caused by the presence of an annular electrode injection window and oxidation aperture can be clearly observed. The current injection close to the oxide aperture rim is stronger than that in the center. The temperature in the active region is the highest. The temperature distribution along the epitaxial direction of the VCSEL at 300 K (heat sink temperature) with different oxide aperture diameters under a fixed current of 3 mA is shown in Fig. 2(b). The VCSEL with an oxide aperture diameter of 3 μm shows a steeper change in temperature along the epitaxial direction and the highest temperature in the active region of approximately 335 K. When the oxide aperture diameter is increased to 10 μm, the temperature changes gently, and the highest temperature is only ∼ 310 K. Importantly, the temperature drop of the device decreases with increasing oxide aperture diameter. The temperature drop is no longer evident when the oxide aperture diameter is larger than 8 μm.

Figure 3 shows the current density and temperature distribution with different oxide apertures at the injection current of 3 mA. Because the two-dimensional axisymmetric model is adopted, the calculated result is the surface current density, which does not affect the conclusion. The heat sink temperature is 300 K. The current density distribution along the R direction in the active layer decreases with increasing oxide aperture diameter [Fig. 3(a)], thereby decreasing the temperature of the active region as the diameter of the oxide aperture increases [Fig. 3(b)]. The insets of Figs. 3(a) and 3(b) represent the changes in current and temperature in the center of the active region with the diameter of the oxide aperture, showing the same trend as that in Fig. 2(b). The temperature and current density drop of the device decrease with increasing oxide aperture diameter and reach saturation when the oxide aperture diameter is larger than 8 μm. As shown in the Fig. 3(b), the temperature of the VCSEL decreases from ∼333 to ∼323 K with the oxide aperture diameter increasing from 3 to 4 μm. When the oxide aperture diameter increases from 8 to 9 μm, the temperature of the VCSEL decrease only from ∼311 to ∼310 K. A too large oxide aperture will lead to a high threshold current of the device, and increase the power consumption of only VCSEL, which is not conducive to the application of VCSELs in chip-scale atomic sensor systems. Therefore, the VCSEL with an 8 μm oxide aperture was finally adopted for experimental verification.

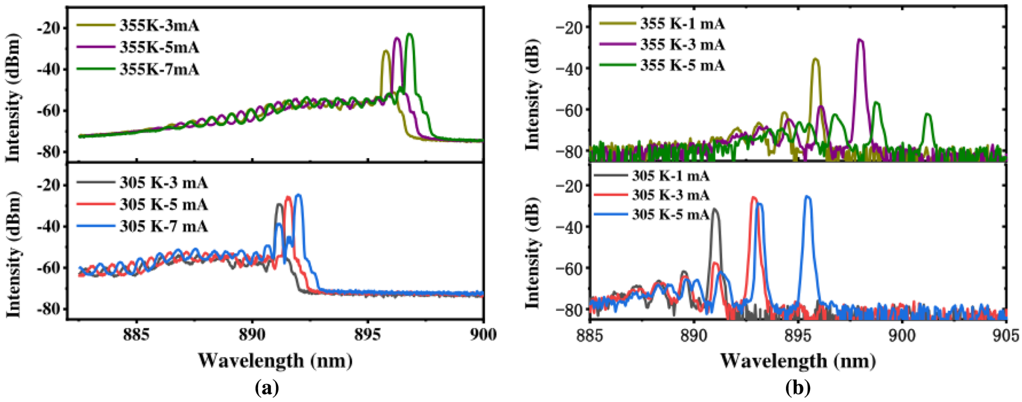

Fig. 4. Spectral characteristics of (a) 8 μm and (b) 3 μm oxide aperture SM-VCSELs at 305 and 355 K.

3. EXPERIMENTAL RESULTS AND DISCUSSION

On the basis of the simulation results, SM-VCSELs with oxide aperture diameters of 3 and 8 μm are prepared, and their performances are compared. The VCSEL is fabricated through a standard process. The mesa and surface relief are formed with inductively coupled plasma reactive ion etching. The etching depth of the relief is 63 nm. The oxide aperture is formed by selectively oxidizing the $Al_{0.98}Ga_{0.02}As$ layer. The SiO_2 insulating layer is deposited by plasma-enhanced chemical vapor deposition. The light-emitting aperture is formed using a lift-off process step. The chip is packaged in a TO56 form, and the heat sink temperature is controlled by TEC. The ambient temperature during the test is room temperature.

The spectral characteristics of the 3 and 8 μm oxide aperture SM-VCSELs at heat sink temperatures of 305 and 355 K are shown in Fig. 4. At 305 K, the VCSEL with an 8 μm oxide aperture can maintain stable single-mode operation when the current is below 7 mA. The side-mode suppression ratio (SMSR) at 7 mA decreases to 13.7 dB as other modes appear. Given the decrease in carrier density in the active region at a high temperature of 355 K, the device can maintain single-mode operation at a current of 7 mA, and the SMSR is 29.92 dB. Some unexcited modes can be seen on the short wave side of the lasing peak in Fig. 4(a) because the surface relief increases the loss of the other modes of the large aperture VCSEL, making them unable to meet the threshold conditions. The VCSEL with a 3 μm oxide aperture can maintain single-mode operation only when the current is less than 3 mA at 305 K. When the current is greater than 3 mA, the high carrier density in the active region makes the high-order transverse mode reach the lasing threshold, and the phenomenon of multi-transverse-mode lasing appears. The optical power of the device decays when the current is greater than 3 mA at 355 K due to thermal saturation [Fig. 4(b)].

The near-field patterns of VCSELs with different oxide apertures measured using an eyepiece with a magnification of 100× are depicted in Fig. 5. To obtain clear near-field patterns and avoid detector saturation, different attenuation rates are used when testing different devices. Figure 5(a) depicts the near fields of VCSELs with 8 μm oxide apertures. The spot profile changes little with temperature. At 7 mA, a primary single-lobe spot can be seen, indicating the single-mode state of the VCSEL. A very

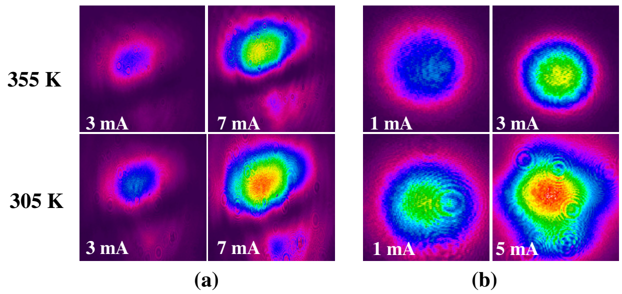

Fig. 5. Near-field patterns of VCSELs with (a) 8 μm and (b) 3 μm oxide apertures at 305 and 355 K.

weak stray light distribution can be seen below the primary spot, representing the unexcited high-order mode, which is consistent with Fig. 4(a). The near-field of a VCSEL with a 3 μm oxide aperture is shown in Fig. 5(b). At 305 K, a single-lobe spot can be seen at low current, while the spot is deformed at high current due to high-order-mode lasing. At 355 K, when the injection current is >3 mA, the output power of the device decreases sharply, resulting in an undetectable near-field spot.

The precise absorption wavelength of the D1 line of alkali metal atom Cs^{133} is 894.6 nm, so the pump source in the atomic sensing system using the Cs^{133} D1 line is required to work at the operating temperature (generally >345 K), and the operation wavelength is near this wavelength. Chip-scale atomic sensing systems, such as atomic clocks and atomic gyroscopes, work by scanning the injection current of the pump source to find the operating wavelengths that match the alkali metal atomic absorption peaks. Figure 6 shows the dependence of the lasing wavelength on the device temperature and injection current of the prepared 8 and 3 μm oxide aperture SM-VCSELs. The temperature and current scanning ranges required to achieve a wavelength variation of 1 nm (894–895 nm) and wavelength accuracy of 894.6 nm are illustrated in Fig. 6(a) (8 μm oxide aperture) and Fig. 6(b) (3 μm oxide aperture), respectively. The SM-VCSEL with a large oxide aperture has a larger temperature–current tunable range. Under the condition of fixed temperature, the wavelength current tuning rate of a large oxide aperture SM-VCSEL is only ∼0.25 nm/mA, in contrast to ∼1.22 nm/mA for the control group with 3 μm apertures. The robustness of this wavelength to current benefits from the

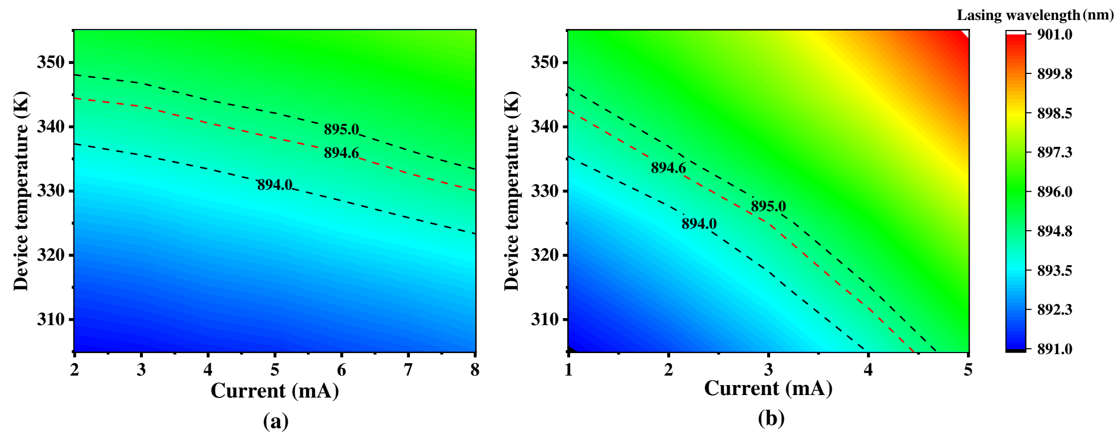

Fig. 6. Dependence of lasing wavelength on device temperature and injection current of (a) 8 μm and (b) 3 μm oxide aperture SM-VCSELs.

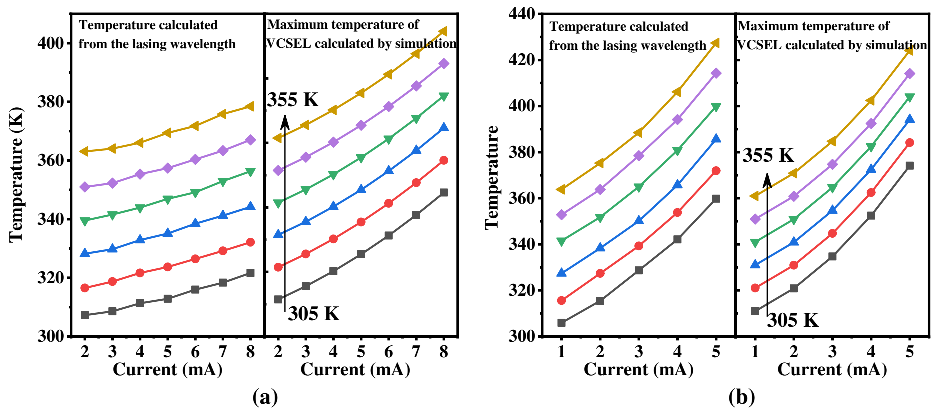

Fig. 7. Temperature variation of (a) 8 μm and (b) 3 μm oxide aperture VCSELs with heat sink temperature and injection current obtained by simulation and experiment.

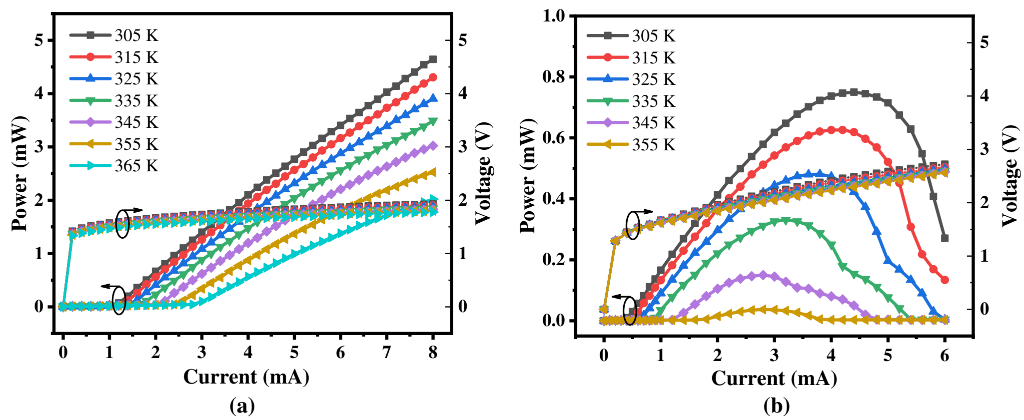

Fig. 8. Power–current characteristics of the (a) 8 μm and (b) 3 μm oxide aperture SM-VCSELs at different temperatures.

low current density and low device heat generation of large aperture SM-VCSEL. This ultra-low wavelength current tuning rate of the VCSEL with an 8 μm oxide aperture is also better than most SM-VCSELs with large oxide apertures (>4 μm), and close to the results of VCSELs with 20 μm oxide apertures and photonic crystal structure, as described in the Introduction.

The temperature coefficient of the wavelength of a GaAs-based VCSEL is ~ 0.06 nm/K [22]. Assuming that when the heat sink temperature is 305 K, and the injection current is at the threshold, the initial temperature of the VCSEL is 305 K, the VCSEL temperature at different heat sink temperatures and injection currents can be calculated according to the lasing wavelength and temperature coefficient of wavelength. Although this hypothesis deviates from the actual temperature of the VCSEL to some extent, the relative temperature change calculated according to the temperature drift characteristics of wavelength is real. Figure 7 shows the comparison of simulation and experimental results of VCSEL temperature with heat sink temperature and injection current. In the simulation results, the maximum temperature point was selected to represent the temperature of the VCSEL, which also deviated from reality to a certain extent, but the trend of temperature change was reasonable. Figure 7(a) shows the temperature variation trend of an 8 μm oxide aperture VCSEL. The simulation results show a stronger tendency for temperature to increase with current than the experimental results. For a 3 μm oxide aperture VCSEL, the agreement between simulation and experimental results is very high, as shown in Fig. 7(b). The possible reason for the deviation of simulation and experimental results when the oxide aperture increases is that the radial area of a fundamental mode light field in a VCSEL with a large oxide aperture is large, and the method of using the highest point of temperature inside the device to represent the overall temperature of the device has a large error. In spite of this error, it can still be found by comparing the temperature change with the current of the VCSEL with two kinds of oxide apertures: both experimental and simulation results show that the device temperature of the VCSEL with an 8 μm oxide aperture shows a more gradual trend with current increase, which is also the reason that the wavelength of the VCSEL has good robustness to current.

Figure 8 depicts the power–current-voltage characteristics of the VCSEL at different temperatures. The threshold current of the 8 μm oxide aperture VCSEL increases from 1.06 to 2.36 mA with the heat sink temperature increasing from 305 to 355 K. The maximum output power of the 8 μm oxide aperture VCSEL at 365 K is 2.02 mW [Fig. 8(a)]. The 3 μm oxide aperture VCSEL has an advantage of low threshold currents [<1 mA, Fig. 8(b)]. However, the output power of the device decreases rapidly with increasing temperature and has almost no output power at 355 K. By fitting the I-V curves, the resistance of a VCSEL with an 8 μm oxide aperture is ∼45 Ω, while that of a VCSEL with a 3 μm oxide aperture is ∼190 Ω. The low resistance reduces the heat generation of the VCSEL for better high-temperature-operation characteristics.

4. CONCLUSION

We demonstrate a high-temperature-operation 894 nm SM-VCSEL with high output power. The influence of oxide aperture diameter on the temperature and current characteristics of VCSELs is studied in detail by simulation and experiment. An important conclusion of the simulation analysis is that although a large oxide aperture diameter helps reduce device temperature, this improvement decreases with increasing aperture diameter. The experimental results show that the VCSEL with an 8 μm oxide aperture can maintain stable single-mode operation at high temperatures. Benefiting from low current density and low device heat generation, the wavelength of a large aperture SM-VCSEL is more robust to current and is more suitable for use as a pump source for chip-scale atomic sensing systems.

Funding. National Key Research and Development Program of China (2018YFB2002400); National Natural Science Foundation of China (11774343, 52172165, 61804151, 61874117, 61874119, 62090060); Jilin Scientific and Technological Development Program (20200401006GX); Jinan Science and Technology Plan (2019GXRC041).

Disclosures. The authors declare no conflicts of interest.

Data availability. Data underlying the results presented in this paper are not publicly available at this time but may be obtained from the authors upon reasonable request.

REFERENCES

1. A. Larson, “Advances in VCSELs for communication and sensing,” IEEE J. Sel. Top. Quantum Electron. **17**, 1552–1567 (2011).
2. A. Kasukawa, “VCSEL technology for green optical interconnects,” IEEE Photon. J. **4**, 642–646 (2012).
3. J. Kitching, “Chip-scale atomic devices,” Appl. Phys. Rev. **5**, 031302 (2018).
4. S. Knappe, V. Gerginov, P. D. D. Schwindt, V. Shah, H. G. Robinson, L. Hollberg, and J. Kitching, “Atomic vapor cells for chip-scale atomic clocks with improved long-term frequency stability,” Opt. Lett. **30**, 2351–2353 (2005).
5. A. Al-Samaneh, M. Bou Sanayeh, M. J. Miah, W. Schwarz, D. Wahl, A. Kern, and R. Michalzik, “Polarization-stable vertical-cavity surface-emitting lasers with inverted grating relief for use in microscale atomic clocks,” Appl. Phys. Lett. **101**, 171104 (2012).
6. N. A. Maleev, S. A. Blokhin, M. A. Bobrov, A. G. Kuz’menkov, M. M. Kulagina, and V. M. Ustinov, “Laser source for a compact nuclear magnetic resonance gyroscope,” Gyrosc. Navig. **9**, 177–182 (2018).
7. D. K. Serkland, K. M. Geib, G. M. Peake, R. Lutwak, A. Rashed, M. Varghese, G. Tepolt, and M. Prouty, “VCSELs for atomic sensors,” Proc. SPIE **6484**, 648406 (2007).
8. M. Grabherr, R. Jäger, R. Michalzik, B. Weigl, G. Reiner, and K. J. Ebeling, “Efficient single-mode oxide confined GaAs VCSELs emitting in the 850 nm wavelength regime,” IEEE Photon. Technol. Lett. **9**, 1304–1306 (1997).
9. J. W. Zhang, X. Zhang, H. B. Zhu, J. Zhang, Y. Q. Ning, L. Qin, and L. J. Wang, “High-temperature operating 894.6 nm-VCSELs with extremely low threshold for Cs-based chip scale atomic clocks,” Opt. Express **23**, 14763–14773 (2015).
10. A. Furukawa, S. Sasaki, M. Hoshi, A. Matsuzono, K. Moritoh, and T. Baba, “High-power single-mode vertical-cavity surface-emitting lasers with triangular holey structure,” Appl. Phys. Lett. **85**, 5161–5163 (2004).
11. H. Dave, Z. Gao, S. T. M. Fryslie, B. J. Thompson, and K. D. Choquette, “Static and dynamic properties of coherently-coupled photonic-crystal vertical-cavity surface-emitting laser arrays,” IEEE J. Sel. Top. Quantum Electron. **25**, 1700208 (2019).
12. D. Zhou and L. Mawst, “High-power single-mode antiresonant reflecting optical waveguide-type vertical-cavity surface-emitting lasers,” IEEE J. Quantum Electron. **38**, 1599–1606 (2002).
13. J. W. Shi, Z. Khan, R. H. Horng, H. Y. Yeh, C. K. Huang, C. Y. Liu, J. C. Shi, Y. H. Chang, J. L. Yen, and J. K. Sheu, “High-power and single-mode VCSEL arrays with single-polarized outputs by using package-induced tensile strain,” Opt. Lett. **45**, 4839–4842 (2020).
14. F. Gruet, A. Al-Samaneh, E. Kroemer, L. Bimboes, D. Miletic, C. Affolderback, D. Wahl, R. Boudot, G. Mileti, and R. Michalzik, “Metrological characterization of custom-designed 894.6 nm VCSELs for miniature atomic clocks,” Opt. Express **21**, 5781–5792 (2013).
15. Å. Haglund, J. S. Gustavsson, J. Vukušić, P. Modh, and A. Larsson, “Single fundamental-mode output power exceeding 6 mW from VCSELs with a shallow surface relief,” IEEE Photon. Technol. Lett. **16**, 368–370 (2004).
16. D.-S. Song, S.-H. Kim, H.-G. Park, C.-K. Kim, and Y.-H. Lee, “Singlefundamental-mode photonic-crystal vertical-cavity surface-emitting lasers,” Appl. Phys. Lett. **80**, 3901–3903 (2002).
17. N. N. Ledentsov, V. A. Shchukin, V. P. Kalosha, N. N. Ledentsov, J.-R. Kropp, M. Agustin, Ł. Chorchos, G. Stępniak, J. P. Turkiewicz, and J.-W. Shi, “Anti-waveguiding vertical-cavity surface-emitting laser at 850 nm: From concept to advances in high-speed data transmission,” Opt. Express **26**, 445–453 (2018).

18. A. Tibaldi, F. Bertazzi, M. Goano, R. Michalzik, and P. Debernardi, "VENUS: a vertical-cavity surface-emitting laser electro-opto-thermal numerical simulator," IEEE J. Sel. Top. Quantum Electron. **25**, 1500212 (2019).
19. H. Li, P. Wolf, X. W. Jia, J. A. Lott, and D. Bimberg, "Thermal analysis of high-bandwidth and energy-efficient 980 nm VCSELs with optimized quantum well gain peak-to-cavity resonance wavelength offset," Appl. Phys. Lett. **111**, 243508 (2017).
20. M. Streiff, A. Witzig, M. Pfeiffer, P. Royo, and W. Fichtner, "A comprehensive VCSEL device simulator," IEEE J. Sel. Top. Quantum Electron. **9**, 879–891 (2003).
21. Ioffe Physico-Technical Institute, "Physical properties of semiconductors," http://www.ioffe.ru/SVA/NSM/Semicond/index.html.
22. http://vixarinc.com/wp-content/uploads/2021/05/V00140.pdf.